Experimental Mechanics
https://doi.org/10.1007/s11340-022-00933-8

RESEARCH PAPER

Fracture-Induced Acoustic Emissions in Gelatin

K. Yerrapragada[1] · D. Chawla[1] · C. R. Henak[1,2,3] · M. Eriten[1]

Received: 25 July 2022 / Accepted: 29 November 2022

Abstract

Background The ever-growing use of soft swollen (multiphasic) materials in engineering and medical applications necessitates monitoring, understanding, and modeling of their mechanical behavior. Energy-to-crack nucleation and propagation are essential in determining load-carrying capacity and toughness of such materials. Therefore, high-throughput and robust testing techniques need to be developed for measuring failure properties of soft swollen materials.

Objective To address the above need, the current study seeks to investigate the acoustic emissions (AE) released from surface cracks on gelatin samples and explore links among AE characteristics and mechanical (mostly failure) properties of the tested samples. In hard materials such as ceramics, composites, and metals, localized indentation cracks generate AE energies proportional to nucleation energies. However, to the best knowledge of the authors, a correlation study between fracture and AE properties on soft swollen materials is currently missing in the literature.

Methods Synchronous Multi-Point Vibrometry (MPV, non-contact) is used to obtain reliable surface wave information (referred to as AE) emitted from cracks induced by quasistatic indentations on gelatin samples. Non-contact sensing of AE from soft materials is essential in eliminating sensor attachment induced mass and stiffness effects.

Results Several properties of the AE signals such as energy, duration, rise time are analyzed and correlated to quasistatic elastic and fracture properties of the gelatin samples.

Conclusions Specifically, a power-law type correlation is found between AE and fracture energies is found for gelatin and compared with hard materials in the literature.

Keywords Acoustic emission · Fracture · Indentation · Gelatin · Surface waves

Introduction

Soft swollen (multiphasic) materials have several applications in traditional and biomedical engineering fields. Hence, it is important to properly understand their mechanical responses. For instance, failure thresholds such as energy-to-crack nucleation and propagation are essential in determining load-carrying capacity and toughness of such materials. *Therefore, high-throughput, minimally invasive and in-operando testing techniques need to be developed for measuring failure properties of soft swollen materials* [1, 2]. The fracture events are often associated with acoustic emissions (AE). AE events detected after fast release of elastic energy have been widely studied in fracture of materials such as ceramics [3], concrete [4], composites [5], and have been utilized in seismic [6, 7] and structural health monitoring [8] applications. In particular, failure-induced AEs are analyzed to obtain quantitative information on crack nucleation [9], crack propagation [10, 11], plastic deformation [12, 13], and dislocation motion [14, 15] in various materials. It is well-known that localized indentation cracks generate AE energies proportional to nucleation energies and toughness of hard materials such as ceramics and metals [16]. The major goal of this study is to explore whether AEs induced locally by indentation cracks can be related to the failure properties of the soft materials. To the best knowledge of the authors, AE- fracture correlation study on soft swollen materials is currently missing in the literature. Here, we fill that gap by addressing common challenges in obtaining reliable vibration data on soft multiphasic, low stiffness materials.

✉ M. Eriten
eriten@wisc.edu

[1] Department of Mechanical Engineering, University of Wisconsin-Madison, Madison, WI, USA

[2] Department of Biomedical Engineering, University of Wisconsin-Madison, Madison, WI, USA

[3] Department of Orthopedics and Rehabilitation, University of Wisconsin-Madison, Madison, WI, USA

Published online: 14 December 2022

Failure properties of soft materials such as elastomers and gels are drawing increased attention due to their increased utilization in load-bearing applications of engineering, food industry and medical fields. Through several numerous microstructural modifications, the toughness and flaw resistance of the soft materials can be enhanced [17–19] to broaden their utility. Hence, measuring and understanding failure properties of those materials are of special importance. Several recent studies focused on understanding fracture mechanisms in soft materials. Zhang et al. [20, 21] used a Y-shaped cutting geometry to investigate the cutting fracture energy response on polydimethylsiloxane (PDMS) with different crosslinks. Milner et al. [22] and Scognamiglio et al. [23] captured multi-crack formations resulting from cavity expansion on soft silicone, ballistic gelatin gels and polymethacrylic acid based hydrogels, respectively. Skamniotis et al. [24] developed finite element models to study the cutting of soft solids. Their cutting force predictions are based on experimentally calibrated viscoplastic law and are shown to be more efficient than the fracture criterion. Duncan et al. [17] explored the fracture energy and crack nucleation energy of soft polymeric gels, i.e. gellan, using razor blade-initiated fracture tests and showed scaling relationships between nucleation, crack energies, and concentration. In addition, our research group studied the fracture mechanisms in porcine cartilage [25, 26] under micro-indentation and discovered that the degree of relaxation in the tissue directly influenced the work to fracture. In the above-mentioned works on soft materials, the primary focus is on understanding the fracture mechanisms.

The main contribution of the current article is to measure crack-induced AEs in gelatin-based hydrogels and relate AE signal properties to samples' fracture properties. We analyze the duration, rise time, and energy of AE signals, and correlate those to quasistatic elastic and fracture properties of the samples. We observe a power-law correlation between AE and fracture energies. Correlation power obtained from gelatin in this study is compared to the ones reported in the literature for hard brittle materials. In addition, we obtained AE signals from nanoindenter-induced fracture of mica, quartz, and aluminum samples. Although those AE signal forms resembled those recorded for gelatin samples, the duration and rise times were approximately four orders of magnitude smaller. The contrast in stiffnesses and thus shear wave speeds of gelatin, mica, quartz, and aluminum samples lead to such stark differences in AE signal properties. These correlations and sensitivity of AE signal properties to samples' elastic and failure properties promise a reliable alternative to mechanical testing of soft swollen materials. The developed study has potential applications in soft materials, such as gelatin based chewable sweets, fresh and frozen vegetables, fruits, pasta, and meat from the food industry, capsules and emulsions in pharmaceutical industry and surgical operations on several biological tissues in medicine. The stiffness and fracture properties of soft materials are directly related to the microstructure and processing conditions. Monitoring of stiffness and failure properties via AEs will enable online quality control of the products and processes.

Indentation-Fracture Experiments

Gelatin samples were prepared at three concentrations 10%, 15%, and 20% (w/V). The details of the sample preparation are given in the Section S1 of the supplementary document. Then, indentation-fracture tests were performed on the samples via a mechanical tester (3230-AT Series III, TA Instruments, New Castle, DE). As demonstrated by the earlier works of the authors, this mechanical tester is ideally suited for indentation-fracture tests on soft materials [25–28]. Gelatin was chosen as a model material system [29] since its properties resemble soft biological tissues with low stiffness [30, 31] and it is widely used in the food industry [32], so its fracture properties are important. The indentation-fracture setup shown in Fig. 1(a) consists of stationary and moving parts. The stationary part includes the crosshead of the tester, a load

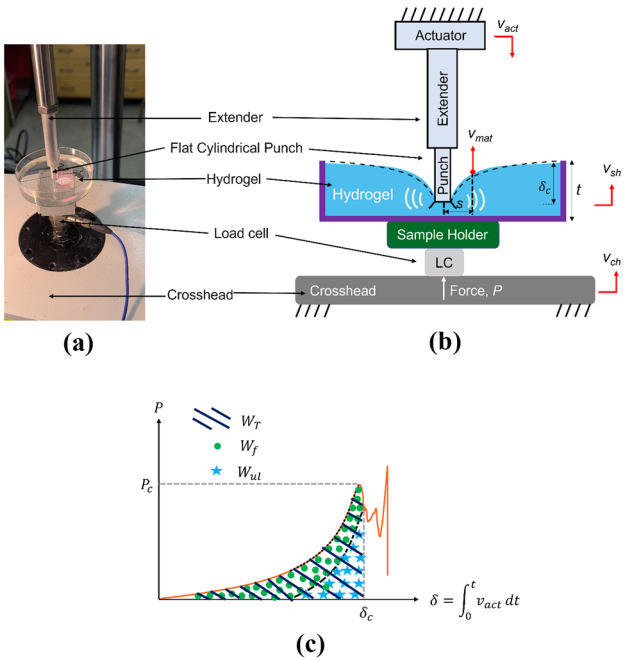

Fig. 1 **a** Experimental Setup of the fracture indentation test on soft material sample using the mechanical tester device and simultaneous recording of acoustic emissions using a MPV device; **b** Schematic of the experiment setup showing the acoustic emission wave profile due to fracture event along with the velocity measurement coordinates; Dotted lines represent the static deformation profile **c** Schematic of the load–displacement curve showing total strain energy W_T, recoverable strain energy W_{ul}, and fracture energy W_f

cell (PCB 208C01 44.48 N), a sample holder, and a petri-dish (6.5 cm inner diameter) holding the cured gelatin stacked on top of the crosshead (Fig. 1(b)). The moving part includes a steel indenter (flat-ended cylindrical punch) that is attached to a linear actuator with the help of a 20 cm steel extender. Further details on the fracture experimental setup are given in the Section S2 of the supplementary document. Fracture events were detected by a rapid drop in the measured load P from the load–displacement profile as shown in Fig. 1(c) on a representative measurement. The noise floor of the load cell is 0.45 mN-rms, which was lower than typical drop off loads (~3 N). The high resolution of the load-cell enables reliable detection of fracture events. The fracture energy W_f was calculated as the shaded area in Fig. 1(c) up to the first major load drop off event, i.e.,

$$W_f = W_T - W_{ul} \tag{1}$$

where $W_T = \int_0^{\delta_c} P d\delta$ is the critical work done by the indenter up to the first fracture nucleation point, and W_{ul} is the recoverable strain energy upon unloading. W_T is computed through trapezoidal integration routine in MATLAB. Note that this work is primarily stored as strain energy in the gelatin samples since the relaxation time constants (~5 s) are greater than loading times (~1 s). Since the fracture events occur stochastically, critical displacements cannot be prescribed before testing, and thus proper unloading and measurement of recovered energy is not possible. To get an estimate of W_{ul}, a hypothetical unloading curve was approximated (cubic interpolation scheme in MATLAB) to begin at the end of first major load drop off (the appropriate section of the loading selected is also shown in Fig. 1(c) through dotted line). The interpolated curve is offset to obtain the unloading curve profile as shown in Fig. 1(c). This approximation assumes that unloading occurs purely elastically and the fracture event does not compromise stiffness of the samples significantly. Finally, the area under that hypothetical unloading curve serves as estimates of W_{ul}. Similar estimations were employed previously by other researchers [33, 34]. Breakdown of critical work, fracture, and recoverable strain energies is shown in Fig. 1(c). The fracture energy W_f is primarily used in the "Correlation between Fracture and Acoustic Emission Energies" section and discussion on the assumptions to calculate W_f is explained there.

Acoustic Emission Monitoring

The fracture events trigger waves (AEs) that propagate outwards from the crack surfaces. At each test, the velocities (v_i) of actuator motion v_{act}, the AEs on the sample surface v_{mat}, the possible vibrations of the sample holder v_{sh}, and the crosshead v_{ch} are monitored simultaneously using a Polytec MPV800 system (Polytec GmbH, Waldbronn, Germany). To achieve synchronization between the fracture and acoustic events, data acquisition in the MPV800 system was triggered at the beginning of the motion of the actuator (indenter). The load cell was connected to a signal conditioner and its output was also synchronously acquired by the data acquisition system of the MPV800. Since AEs are rapid events (short time transients), the data was acquired at 100 kHz. Cracks under flat-ended indenters were expected to nucleate and propagate in the vicinity of the indents due to stress concentrations [35]. Therefore, proximity of sensing locations to the indent locations was essential for detectable AE signal strength. The sensing locations on the samples were 1.5 mm and 3 mm from the edge of the 1.5 mm and 3 mm radii (3 mm and 6 mm diameter) indenters, respectively. This ensures the same $\frac{s}{r} = 2$ ratio for both indenter cases, where s is the distance of the sensing location of v_{mat}, from the center of the indenter and r is the radius of the indenter. The typical wave speeds of gelatin are of the order of 5 m/s (shown later in Fig. 5(d)), considering sample radius of 32.5 mm, wave frequencies of the order of 50 Hz, the resulting wave lengths of the AE suggests we expect standing waves in the sample that are localized to the surface. Considering the continuous vibration (distributed parameter) system [36], the frequencies of the lower modes are expected to be in the range of 40–200 Hz. The spatial profile of the standing waves follows a Bessel function of first kind where the peak amplitude occurs near the center boundary condition and reaches zero at the fixed boundary condition. For the first mode, there will be no nodal circles or nodal diameters. As the mode number increases, we start to observe nodal circles and diameters. In soft materials, we typically expect the higher vibration modes to quickly attenuate, and we mostly observe the lower modes. Therefore, for a given mode shape with no risk of nodal point for sensing, the choice of sensing location can alter the velocity magnitudes measured but will not influence the correlation powers (acts only as a scalar shift in AE energy). For instance, if the sensing location approaches closer to the fixed boundary (nodal point for the first vibration mode), the velocity magnitude we measure decreases as expected. In nanoindentation-induced fracture tests on hard materials, the acoustic emission frequencies are very high (~MHz) as wave speeds (3–4000 m/s, shown later in Fig. 5(d)). Although the resulting wave lengths are small (few mm), we also expect standing waves since the samples are small as well. One advantage of those studies overcoming possibility of nodal location at sensing is that in nanoindentation-induced cracks, the piezo-based AE sensor is embedded in the probe and thus will always measure the AE signal reliably. Such a probe configuration is challenging for soft materials as the softness require low

frequency sensing and currently available piezo-based sensors do not fulfill the requirement.

To mark the sensing locations and enhance laser reflectivity, titanium dioxide (TiO_2) powder (Loud Wolf Industrial and Scientific, 44 microns, 99.9% pure) was applied at the sensing locations with a 3D-printed mask plate having the exact diameter as the petri dish [37]. Hydrogels are transparent and thus do not reflect the incident laser beam with small wavelengths that are used by conventional laser doppler vibrometers. Recently, a laser beam with larger wavelengths (NIR wavelengths at 1550 nm) has been successfully used to study vibration of gelatin disks [38, 39]. The MPV800 system uses similar wavelengths and thus ensures proper reflectivity. Besides, the titanium dioxide marks enhance reflectivity and signal strength further. With those enhancements, the noise floor of the MPV800 was measured as 0.1 mm/s. Thus, both the actuator motion at prescribed loading rates (2.5 and 5 mm/s) and maximum typical AE velocities (> 3 mm/s) are monitored with high signal-to-noise ratio. In addition to the actuator motion, AEs on the sample surface; the motion of the sample holder and crosshead are also monitored simultaneously during each test to quantify the portion of the AE energy localized on the samples versus the portion being transmitted to the neighboring parts. For each measurement, corresponding angle between the laser beam and the normal vector to the measured surface is used to calculate normal components of vibrations.

Figure 2 shows representative time series obtained from an indentation-fracture test. In particular, Fig. 2(a) illustrates the indentation load zoomed around the first major fracture event detectable as a clear load drop off. The corresponding load–displacement curve shown in Fig. 1(c) also features that clear drop off. Figure 2(b) shows the velocities measured by the MPV800 system. The velocities of the sample holder v_{sh} and the tester's crosshead v_{ch} are negligible compared to the material response v_{mat}. The material response resembles a clear burst at the time of fracture followed by decaying transient vibrations. The dynamic strains associated to the maximum velocities experienced during burst portion are on the order of 0.5%. Therefore, linearized dynamic analysis is applicable to the experiments. Each indentation-fracture test induces both volumetric and deviatoric strains in the gelatin samples and thus the sudden release of strain energy due to fracture is expected to emit both longitudinal and shear waves. Considering that longitudinal wave speed in gelatin is close to the speed of sound in water (~1500 m/s [40]), the measured range of frequencies correspond to wavelengths on the order of 10 m, which is significantly larger than the sample diameter (65 mm). Given that the gel is expected to stick to the petri dish walls, a fixed boundary condition is a good approximation for wave reflections and vibrations. So, detecting longitudinal wave reflections and resulting oscillations on the sample surface requires sampling frequencies

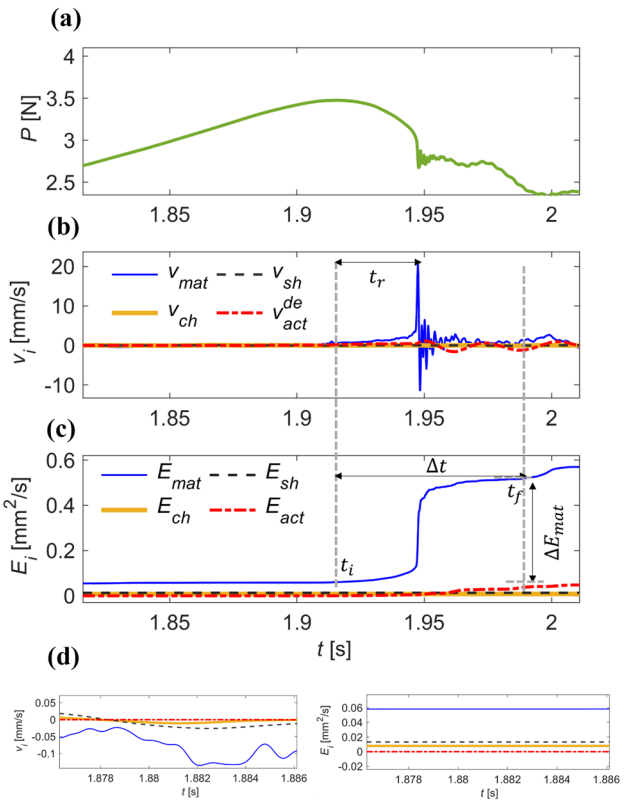

Fig. 2 **a** Experimental data of the load profile showing the time of the fracture event; **b** Corresponding acoustic emissions due to fracture event; **c** Cumulative acoustic energy build up due to the fracture event; **d** Inset plots of velocity and acoustic energy build up before fracture

on the order of MHz, which is beyond the current capabilities of the MPV800 system. Thus, in this work the focus is on the shear component of the surface waves. A typical AE wave form in gelatin samples is shown in Fig. 2(b). The AE occurs at the time of load drop off. The AE wave form resembles modulated oscillations decaying after the peak value is reached.

At each fracture event, some vibrations are measured also on the actuator side, v_{act}, shown as the detrended signal, $v^{de}_{act} = v_{act} - \dot{\delta}$ during the loading cycle in Fig. 2(b). This is another evidence that fracture events are localized to the tip of the indenter and sudden drop in the load triggers structural modes of the actuator and controller system (moving parts of the setup) as well. The frequency content on the actuator side is much lower than the sample vibrations as the actuator has an electromagnetic linear motor and an active controller that corrects for any external disturbance, especially high frequency ones. Therefore, the following AE properties will primarily be extracted from the material response and the wave perturbations observed on the actuator side are ignored in the further analysis.

The acoustic energy accumulated during each experiment is calculated as done elsewhere [41, 42], equation (2).

$$E_i = \int_0^t v_i^2 dt \tag{2}$$

where i is *mat, sh,* and *ch*. For the case of actuator, the detrended signal $\int_0^t \left(v_{act}^{de}\right)^2 dt$ is used to compute the energy E_{act} in Fig. 2(c). Several works related to acoustic emission due to fracture find the cumulative energy by integrating the square of the response of the signal in time [4, 6, 41–43]. In the literature, most of the acoustic sensors are contact based and work on the principle of piezoelectricity where the sensor provides output in the form of voltage for a given mechanical strain (in the form of waves). The mentioned works used the electrical signal (voltage units) to understand the mechanical phenomena (wave emissions) as the strains and voltage are related to each other. The potential and kinetic energy of the wave is related to the displacement, velocity, and material parameters such as moduli and density [44]. In the current work, the velocity of the signal is measured. The kinetic energy density of the wave of distributed parameter system at a particular location is proportional to $\rho \dot{u}(l,t)^2$. Since, in this study one material (gelatin) is considered with concentrations in the range of 10% (w/V) to 20% (w/V), the density change across this concentration range is negligible (1.02 times, supplementary document of [38]). Therefore, we consider the instantaneous acoustic energy or kinetic energy from the surface wave scale as the square of the velocity $\dot{u}(l,t)^2 \left[mm^2/s^2\right]$ and once integrated over the total event time, that quantity scales with the cumulative acoustic energy $\left[mm^2/s^2\right]$.

The representative build-up of acoustic energy is shown in Fig. 2(c) for all the signals measured from 3 mm diameter indenter and 15% (w/V) concentration case at 2.5 mm/s loading rate. The displacement of the testing device is controlled by a PID controller (second order system). Hence, when the actuator starts from the rest and reaches a constant loading rate, some overshoot and oscillations occur within the actuator-indenter system (structural modes). The system quickly settles into steady state within 0.1—0.2 s after initiation of loading. Because of that initial disturbance, the cumulative energy from equation (2) shows some acoustic buildup which then settles into non-zero value as observed in signals of Fig. 2(b). A zoomed in inset plot is also attached as Fig. 2(d) showing some of the offset values. In addition, the material initially experiences static deformation at the sensing location due to quasistatic indentation which also results in some acoustic buildup before fracture. However, the static deformation quickly relaxes and therefore before the fracture we observed low velocity magnitude of the material. As expected from negligible velocities v_{sh} and v_{ch} measured on the sample holder and the crosshead, corresponding acoustic energies E_{sh} and E_{ch} were close to zero. In contrast, the change in the acoustic energy corresponding to the fracture event was substantial in the signal measured on the material (E_{mat} in Fig. 2(c)). That change was quantified as

$$\Delta E_{mat} = E_{mat}\left(t_f\right) - E_{mat}\left(t_i\right) \tag{3}$$

where t_i and t_f are the initial and end times of the fracture event. The initial time is chosen when the signal deviates from the base level by 15%. The rise time t_r is also shown in Fig. 2(b) as the time for the signal to reach a peak amplitude value from the base noise level and the cumulative acoustic energy E_{mat} also increases from the base level in Fig. 2(c). The final time is set when the crack arrest happens, and the cumulative acoustic energy buildup reaches a constant value. From Fig. 2, during the first crack event we observe a sharp increase in the cumulative acoustic energy, Mathematically, this would indicate a sudden increase in the slope dE_{mat}/dt during the crack event and there is negligible in the acoustic energy buildup after that (second decimal change). From load displacement plot in Fig. 1(c), we observe multiple crack events. So, before the second fracture event the dE_{mat}/dt again starts to increase. After the first sharp increase during the first crack event, the acoustic emission vibrations settle down to noise level and the slope dE_{mat}/dt almost drops to $< 5mm^2/s^2$. Considering the ambient noise level, the values of the slope vary between $1 to 5 mm^2/s^2$ when the vibrations dampen out. The peak values of slope at the crack event are in the range of 400 mm^2/s^2. So, the slope values reach to about 0.01 times the peak value after the waves settle down. As in this study we are primarily interested in the acoustic emission at the first crack event, the t_f can be taken until the slope dE_{mat}/dt reaches to the above mentioned low levels and we also observe the waves dampening out. The total duration of the signal before the rise time to the end of the AE event is estimated as $\Delta t = t_f - t_i$ as shown in Fig. 2(b). In addition, the cumulative energies from the sample holder and crosshead are close to zero, confirming that they do not have any significant motion during the fracture events. As explained for Fig. 2, the fracture event leads to rapid buildup of cumulative acoustic energy. Based on the counts defined in [11], the number of times a signal crosses the noise threshold, the average frequency is estimated as $f_{avg} = {}^{\text{Counts}}/_{\Delta t}$ [45, 46]. Based on the order of vibration frequencies of v_{mat} reported in this work (~10^2Hz) and shear wave speeds of gelatin reported as several m/s [47], we estimate the wavelengths to range from 15 to 75 mm, which is comparable to diameter of the samples used in the experiments. Therefore, the AEs reported in this work primarily consist of shear waves in the form of transverse vibrations of the surface. Losses due to viscoelasticity of the gelatin samples are responsible after decaying transients observed. Due to the low stiffness of hydrogels (< 150 kPa modulus), non-contact sensing of wave emissions is essential in eliminating attachment induced effects such as added mass and stiffness of contact-based sensors (accelerometers, strain gauges, etc.).

Analysis of Fracture Properties

For each combination of indenter size (3 and 6 mm), loading rate (2.5 and 5 mm/s) for a given concentration, four samples were tested. In the current gelatin experiments, the loading rates were restricted to 2.5 and 5 mm/s; as the loading rates in this range ensure proper synchronization between the acoustic sensing system and the mechanical tester. For 10%, 15% and 20% (w/V), for the combination of the indenter sizes and loading rates, 16 samples each are tested. Fourty six samples fractured out of the 48 samples tested and 33 samples are retained for analysis. The remaining samples which either did not show rapid buildup of the acoustic energy or fractured close to the transition between the end of loading cycle and relaxation period or which produced acoustic energy at sensor noise level were omitted for further analyses. When the selected experimental configurations and sample concentrations are combined, more than an order of magnitude variation in critical work to fracture W_T and fracture energy W_f is obtained (Fig. 3(a)). The concentration of the gelatin material investigated were 10%, 15% and 20% (w/V). The strains for the first fracture event are in the range of 60 to 80%, similar to other fracture studies on gels [32]. The variation in critical load for combinations of different concentrations, indenter sizes produce a range of total strain and fracture energies of the samples. Figure 3(a) shows that the critical strain energy W_T scales almost linearly with the fracture energy W_f, $W_f \propto W_T^{0.95}$ ($R^2 = 0.95$) and approximately 25% of the critical work is fracture energy in gelatin samples. Tymiak et al. [42] conducted similar analysis on brittle materials and reported $W_f \propto W_T^{0.35}$, $W_f \propto W_T^{0.37}$ and $W_f \propto W_T^{0.35}$ with $R^2 = 0.89, 0.87, 0.85$, respectively for MgO, W and Sapphire.

Representative bright field images of the cracked zone are shown in Fig. 3(b) (i) and (ii) for the 3 mm and 6 mm indenter cases, respectively. Those images are taken for two 20% (w/V) samples. India ink was applied on the cracked surface to stain the crack morphology and then was gently wiped off. The fractured hydrogel surfaces were then imaged using an inverted microscope (IX-71, Olympus, Tokyo, Japan). Tilescan images at 10X were used to visualize any additional damages other than the site of fracture. The indenter area corresponding to 3 mm and 6 mm diameter size is shown as dotted circles in Fig. 3(b) (i) and (ii) respectively. The cracks possessed a rather complicated geometry evident by sporadic and dense distribution of inked islands beneath the indented area. Due to instrument's limitation, the samples could not be imaged in the thickness direction and therefore the exact crack geometry cannot be obtained. To obtain an approximate fracture toughness, we set the crack area to the product of indenter perimeter and critical displacement, i.e., $A_{cr} = \pi d \delta_C$. Similar approximation to crack areas is commonly employed in needle insertion experiments (see for instance Gokgol et al. [48] studying fracture toughness of liver samples via needle insertion). Fracture toughness values estimated by W_f/A_{cr} range from 15 J/m^2 for 10% (w/V) samples to 149 J/m^2 for 20% (w/V) samples. Those values are in line with the values reported in the literature. For instance, Misra et al. [49] conducted needle-insertion tests at 2.5 mm/s insertion speed (comparable to our indentation speeds) and reported a rupture toughness of 82.28 J/m^2 for 15% (w/V) porcine gel and 115.40 to 221.04 J/m^2 for soft to stiff plastisol gels. Forte et al. [50] conducted wire-cutting tests and reported 15 J/m^2 for 10% (w/w) gelatin at cutting speeds comparable to the indentation rates we used. The fracture toughness values for porcine and bovine-based gelatins were obtained by puncture tests in [32] ranging from 6 to 40 J/m^2 proportional to the gel concentrations from 10 to 33% (w/V). This last set of data, however, was obtained at 5 mm/min, so 60 times slower than our indentation speeds. Note that Forte et al. [50] showed that apparent fracture toughness values scale with square root of cutting speeds. They explained this rate-dependent toughness with poroelastic effects; i.e., water diffusion due to pressure changes in the fracture process zone. Assuming similar relation is applicable to puncture (indentation-fracture) tests, we expect a $\sqrt{60} \sim 7.75$ fold increase in fracture toughness values reported in [32] when puncture speeds approach ours. Such a scaling pushes their range to [46.5, 310] J/m^2, which is more consistent with what we and others observed for similar gels under comparable loading rates. Overall, the measured fracture toughness values are apparent estimates that depend on gel concentration and loading rates.

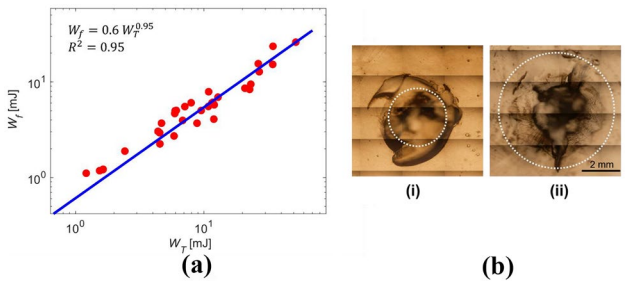

Fig. 3 **a** Relation between the critical work W_T and fracture energy W_f for gelatin samples; **b** Representative bright field crack image for the (i) 3 mm and (ii) 6 mm indenter cases respectively, the indenter areas are shown as dotted circles

Correlation between Fracture and Acoustic Emission Energies

The fracture-induced changes in acoustic energies on the material ΔE_{mat} are plotted against corresponding fracture energies W_f and total strain energies W_T in Fig. 4(a) and (b).

The noise floor of the MPV system is 0.1 mm/s, and thus the lowest energy level that can be measured by the MPV 800 device is around 10^{-3} mm^2/s for typical signal durations. The lowest acoustic energy ΔE_{mat} shown in Fig. 4 is 0.08 mm^2/s and thus all reported AE energies are orders of magnitude higher than noise floor. Combination of sample concentrations and experimental configurations resulted in approximately an order of magnitude variation in fracture energies. Larger concentrations and indenter sizes produced larger fracture energies and resulted in larger acoustic energies. The measured acoustic energies depend on several parameters, such as the amplitude, rise time, time duration and the frequency component of the wave. We observed close to 40-fold increase in ΔE_{mat}. The change in acoustic energy follows a power law (curve-fit) with the fracture energy, $\Delta E_{mat} \propto W_f^{1.02}$ ($R^2 = 0.92$), where we refer to 1.02 as the correlation power.

The correlation of acoustic energy with total strain energy is also shown in Fig. 4(b). The total strain energy correlates with a power of 0.98 with ($R^2 = 0.92$). Both correlations are strong and yield similar power laws. Note that the total strain energy W_T calculations involve no specific assumptions while fracture energy estimations assume fully elastic unloading curve (offset translation method). Despite being used elsewhere on various samples and failure mechanisms (Refs. [3, 42]), that assumption will be violated when the failure is large and dissipative response of samples cannot be neglected. In that regard, correlations of AE energies with W_f and W_T correspond to two asymptotic cases: fully elastic and fully lossy (poroviscoelastic) material response, respectively during hypothetical unloading after the failure. Similar correlation analysis are reported for hard materials in the nondestructive testing and evaluation literature as summarized in Table 1. Most of the AE studies in Table 1 measured waves with the acoustic sensors embedded in the actuator. In Chen et al. [51] independent sensors are placed on the concrete material. Tymiak et al. [33] also attached an independent sensor to record the AE in MgO. However, the

Table 1 Comparison of correlation powers and type of acoustic emission sensing between gelatin and various synthetic brittle materials

Material	AE detection	Correlation Powers	R^2
Gelatin (Current Work)	Independent	1.02	0.92
MgO and W [33]	Embedded	1.23	0.95
Sapphire [33]	Embedded	1.54	0.95
Si based materials [54]	Embedded	1.29	0.68
MgO, Al_2O_3 and LTCC [55]	Embedded	1.63	0.99
Fe-3Si and Ta_2N [3]	Embedded	2.11	0.95
Concrete, Mortar [4]	Embedded	2.20	0.55
Concrete [51]	Independent	1.18	0.81

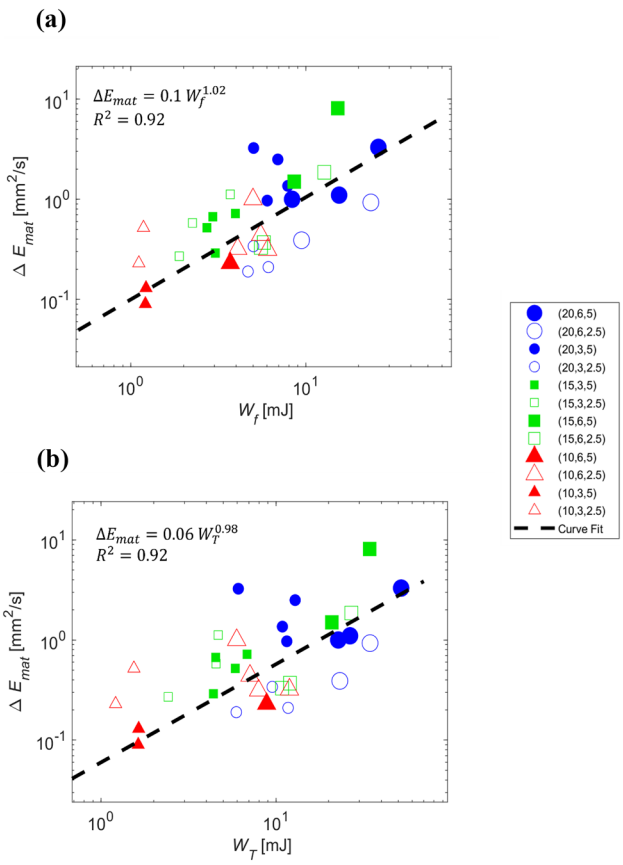

Fig. 4 Correlation between the AE energies and **a** Fracture energy **b** Total strain energy. In the legend representation, concentration, indenter diameter and loading rate are shown in (c %,d mm, $\dot{\delta}$ mm/s)

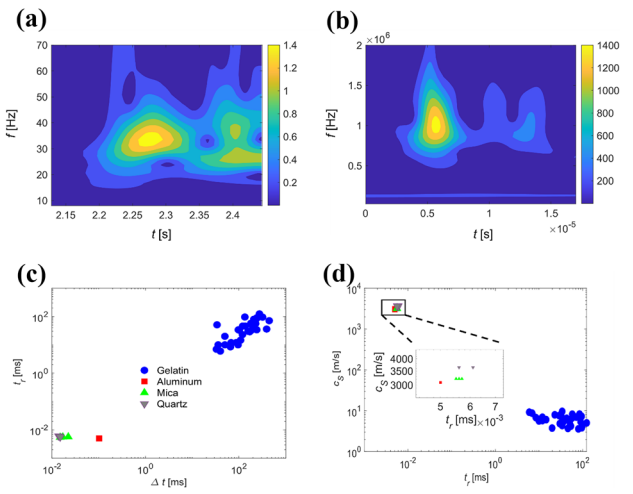

Fig. 5 Wavelet transform of the AE events for **a** Gelatin 10% (w/V); **b** Mica showing the burst of AE; **c** Relation between the rise time and time duration of the AE signal for gelatin and for hard materials; **d** Relation between the shear wave speed and the rise time

independent contact sensor resulted in very low signal to noise ratio with significantly altered wave forms compared to the embedded sensor. Also, the independent sensor only had 67% success rate in capturing AE on hard materials [33]. Gelatin samples have low stiffness, for such samples, non-contact sensors are the only feasible way to accurately capture the AE events as demonstrated here.

Correlations as in Fig. 4 between AE source properties and received data are broadly studied in geomechanics. Specifically, seismograms deliver the received data from which information about fault kinematics and kinetics is sought after [52]. In that field, certain percentage of elastic strain energy released during fault fracture or slip is known to radiate seismic waves. Besides, both the released energy and far-field displacements due to radiated waves can be equivalently related to seismic moments. Analytical correlations between released energy and measured displacements require accurate knowledge of dynamic source function, Green's function for the studied material under realistic boundary and preload conditions and response transfer function that converts wave displacements to measured signals [53]. In our tests, the MPV800 delivers velocities directly so the response transfer function is not needed. Besides, both the lateral dimensions and thickness of the gelatin samples are comparable to the wavelengths and hence, dynamic Green's function would entail vibration modes of the gelatin layers. However, our tests cannot resolve the dynamic source function spatially. As shown in Fig. 3(b), the crack geometry evolves in an asymmetric way beneath the indenter and crack size is comparable to the wavelengths, and thus point source assumption would be erroneous. Therefore, an analytical solution that links source kinematics and energetics to the measured displacements is not possible. Alternate methods to monitor the spatiotemporal evolution of crack area experimentally and integrating it into dynamic finite element simulations would be necessary to provide that link.

Acoustic Emission Properties

In this section, additional analyses on the measured AE signal properties are reported. For the AE signal corresponding to a representative gelatin sample, the continuous wavelet transform was computed using the cwt function of the MATLAB signal processing toolbox. More details about the cwt command are given in Section S4 of the supplementary document. The time resolution of the wavelet for the gelatin samples was 10^{-5} s.

The dominant frequency contours for the softer gelatin can be observed around 40 Hz for the given concentration in Fig. 5(a). The wavelet transform shows the sudden burst of acoustic energy near the fracture event in the form of multi frequency components. The wavelets are shown near the time where the AE release has occurred due to the fracture event. During the acoustic event the frequencies also vary with time. The color bar in Fig. 5(a) represents the magnitude of the wavelet, and the units of magnitude for Fig. 5(a) are mm/s. The dominant contours vary from 30 to 250 Hz. The variation of frequency with time depends on the parameters such as concentration, loading rates. In most of the studies related to AE, the average frequencies are usually reported and estimated using counts as explained earlier in AE monitoring section. The average frequencies based on counts estimation, f_{avg} range from 20 to 120 Hz for the samples studied.

To compare the AE properties of gelatin with hard materials (mica, quartz and single crystal aluminum; material properties [56]), we conducted an independent set of nanoindentation-fracture experiments. The details of the nanoindentation experiments are given in Section S3 of the supplementary document. The data for the nano-indentation experiments are acquired at 10 MHz. A representative AE signal from mica is shown in Fig. 5(b) (corresponding time series is shown in Supplementary Fig. 1(B)). For Fig. 5(b), hard material response, the units of wavelet magnitude are related to voltage. The hard material acoustic emission responses are recorded using piezo based sensor which provides output in the form of voltage. The frequency range for the harder material sample mica are of the order 10^6 Hz as shown in Fig. 5(b). Quartz (refer Supplementary Fig. 2(A) for wavelet transform) and mica are brittle materials and show similar type of localized energy bursts around the fracture event as gelatin samples. The aluminum shows ductile failure trend (see Supplementary Fig. 2(B) for wavelet transform) where the AEs are spread across larger time duration than the brittle materials. On a global material moduli scale, the high young's moduli (~GPa) of the hard materials result in AE with larger dominant frequencies (~MHz) and relatively softer brittle gelatin material (~kPa) results in lower AE frequencies (~Hz). About four orders of magnitude variation in rise time between gelatin and hard materials was observed (Fig. 5(c) and (d)). From Fig. 5(c), the acoustic events happen faster (Δt) in hard materials faster than the softer materials; In gelatin as well, the rise time is proportional to the time duration. From Fig. 5(b), hard brittle material releases waves with very high frequency (~MHz), so we observe the rise time and duration of the micro-seconds. From Fig. 5(a) for the gelatin samples the frequencies are of the order of (~Hz) and Δt, t_r are relatively higher. The shear wave speed of the materials can be determined from the moduli value by $c_S = \sqrt{G/\rho}$ where G is the shear modulus and ρ is the density. The shear modulus can be determined with a Poisson's ratio assumption of 0.4 for gelatin samples [38]. The relation between the material wave speeds and rise time shown in Fig. 5(d), we observe inverse proportionality where the materials with larger shear wave speed

have smaller rise time due to high frequency content of the shear waves. If one knows the densities of tested materials, Fig. 5(d) suggests that the elastic properties of the gelatin such as shear modulus can also be linked to AE properties such as rise time.

Conclusion

In this article, we developed a correlation between the fracture and acoustic energies in gelatins, motivated by industrial (food, engineering and medical) applications. Hydrogels were synthesized with three different concentrations. Flat cylinder-based indentation experiments were performed on various gel concentrations, loading rates and indenter size combinations. The fracture events resulting from the indentation experiments emitted surface waves in the soft material samples. The shear component of the AE was captured using a non-contact laser vibrometer with a high sampling frequency. Initially, the fracture properties of all the samples are analyzed, and the samples fractured at several critical loads depending on the loading conditions. The critical work to fracture and the fracture energies are observed to have a linear relationship in the studied gelatin samples. Then, the acoustic energies (equivalent kinetic energy) are computed from the velocity signals of the material sensing location. The acoustic energy is found to increase with the fracture energy with almost linear relationship in the studied gelatin material. The correlation power from this study is also compared with several other published studies on harder materials such as concrete, ceramics etc. which had slightly higher powers. Several AE properties such as the rise-time, time duration and frequency of the gelatin samples are obtained and compared with another independent set of fracture-induced AE experiments on hard materials like mica, quartz, and aluminum. Harder materials have four orders of magnitude lower rise time than gelatin samples. The current study also demonstrates the importance of using non-contact sensors in soft hydrogels (due to their low stiffness) to accurately monitor the AE events. It is important to obtain information about fracture properties of the products in several clinical and food applications, the conducted study forms as a basis of motivation to predict the fracture energies in soft swollen gelatin-based hydrogels based on the acquired AE events.

Supplementary Information The online version contains supplementary material available at https://doi.org/10.1007/s11340-022-00933-8.

Funding This research related to the intellectual property is partially funded by the US National Science Foundation (award numbers: CMMI-DCSD-1826214, CMMI-DCSD-2200353, CMMI-DCSD-1662456) and University of Wisconsin, Madison: (PARCI, Vilas Life Cycle).

Data Availability The datasets generated and analysed during the current study are available from the corresponding author on reasonable request.

Declarations

Conflict of Interest The authors declare no conflict of interest in the preparation of this article.

References

1. Boz U, Eriten M (2019) Nonlinear system identification of soft materials based on Hilbert transform. J Sound Vib 447:205–220
2. Dalisay JDE, Liu L, Eriten M, Bergman LA, Vakakis AF (2022) Characterization of visco-hyperelastic behavior of open cell polyurethane foam through transient shear testing. Int J Solids Struct 241:111482
3. Bahr DF, Gerberich WW (1998) Relationships between acoustic emission signals and physical phenomena during indentation. J Mater Res 13(4):1065–1074
4. Landis EN, Baillon L (2002) Experiments to relate acoustic emission energy to fracture energy of concrete. J Eng Mech 128(6):698–702
5. Bussiba A, Kupiec M, Ifergane S, Piat R, Böhlke T (2008) Damage evolution and fracture events sequence in various composites by acoustic emission technique. Compos Sci Technol 68(5):1144–1155
6. Lockner D (1993) The role of acoustic emission in the study of rock fracture. Int J Rock Mech Min Sci Geomech Abstr 30(7):883–899
7. Goodfellow SD, Young RP (2014) A laboratory acoustic emission experiment under *in situ* conditions. Geophys Res Lett 41(10):3422–3430
8. Cawley P (2018) Structural health monitoring: Closing the gap between research and industrial deployment. Struct Health Monit 17(5):1225–1244
9. Ohtsu M, Ono K (1988) AE source location and orientation determination of tensile cracks from surface observation. NDT Int 21(3):143–150
10. Kral Z, Horn W, Steck J (2013) Crack propagation analysis using acoustic emission sensors for structural health monitoring systems. Sci World J 2013:823603
11. Chang H, Han EH, Wang JQ, Ke W (2009) Acoustic emission study of fatigue crack closure of physical short and long cracks for aluminum alloy LY12CZ. Int J Fatigue 31(3):403–407
12. Nowak R, Sekino T, Maruno S, Niihara K (1996) Deformation of sapphire induced by a spherical indentation on the (1010) plane. Appl Phys Lett 68(8):1063–1065
13. Trochidis A, Polyzos B (1994) Dislocation annihilation and acoustic emission during plastic deformation of crystals. J Mech Phys Solids 42(12):1933–1944
14. James DR, Carpenter SH (1971) Relationship between acoustic emission and dislocation kinetics in crystalline solids. J Appl Phys 42(12):4685–4697
15. Heiple CR, Carpenter SH, Carr MJ (1981) Acoustic emission from dislocation motion in precipitation-strengthened alloys. Met Sci 15(11–12):587–598
16. Faisal NH, Ahmed R, Reuben RL (2011) Indentation testing and its acoustic emission response: applications and emerging trends. Int Mater Rev 56(2):98–142
17. Duncan TT, Sarapas JM, Defante AP, Beers KL, Chan EP (2020) Cutting to measure the elasticity and fracture of soft gels. Soft Matter 16(38):8826–8831
18. Mredha MTI, Jeon I (2020) High-water-content hydrogels exhibiting superior stiffness, strength, and toughness. Extreme Mech Lett 37:100691

19. Li Z, Liu Z, Ng TY, Sharma P (2020) The effect of water content on the elastic modulus and fracture energy of hydrogel. Extreme Mech Lett 35:100617
20. Zhang B, Hutchens SB (2021) On the relationship between cutting and tearing in soft elastic solids. Soft Matter 17(28):6728–6741
21. Zhang B, Shiang CS, Yang SJ, Hutchens SB (2019) Y-shaped cutting for the systematic characterization of cutting and tearing. Exp Mech 59(4):517–529
22. Milner MP, Hutchens SB (2021) Multi-crack formation in soft solids during high rate cavity expansion. Mech Mater 154:103741
23. Scognamiglio C, Magaletti F, Izmaylov Y, Gallo M, Casciola CM, Noblin X (2018) The detailed acoustic signature of a micro-confined cavitation bubble. Soft Matter 14(39):7987–7995
24. Skamniotis CG, Charalambides MN (2020) Development of computational design tools for characterising and modelling cutting in ultra soft solids. Extreme Mech Lett 40:100964
25. Han G, Eriten M, Henak CR (2019) Rate-dependent crack nucleation in cartilage under microindentation. J Mech Behav Biomed Mater 96:186–192
26. Han G, Chowdhury U, Eriten M, Henak CR (2021) Relaxation capacity of cartilage is a critical factor in rate-and integrity-dependent fracture. Sci Rep 11(1):1–12
27. Chawla D, Han G, Eriten M, Henak CR (2021) Microindentation Technique to Create Localized Cartilage Microfractures. Curr Protoc 1(10):e280
28. Hwang JW, Chawla D, Han G, Eriten M, Henak CR (2022) Effects of solvent osmolarity and viscosity on cartilage energy dissipation under high-frequency loading. J Mech Behav Biomed Mater 126:105014
29. Ozkaya E, Triolo ER, Rezayaraghi F, Abderezaei J, Meinhold W, Hong K, Alipour A, Kennedy P, Fleysher L, Ueda J, Balchandani P (2021) Brain-mimicking phantom for biomechanical validation of motion sensitive MR imaging techniques. J Mech Behav Biomed Mater 122:104680
30. Budday S, Ovaert TC, Holzapfel GA, Steinmann P, Kuhl E (2020) Fifty shades of brain: a review on the mechanical testing and modeling of brain tissue. Arch Comput Methods Eng 27(4):1187–1230
31. Chawla D, Kaur T, Joshi A, Singh N (2020) 3D bioprinted alginate-gelatin based scaffolds for soft tissue engineering. Int J Biol Macromol 144:560–567
32. Czerner M, Fasce LA, Martucci JF, Ruseckaite R, Frontini PM (2016) Deformation and fracture behavior of physical gelatin gel systems. Food Hydrocoll 60:299–307
33. Tymiak NI, Daugela A, Wyrobek TJ, Warren OL (2004) Acoustic emission monitoring of the earliest stages of contact-induced plasticity in sapphire. Acta Mater 52(3):553–563
34. Wu H, Zhao G, Liang W (2019) Investigation of cracking behavior and mechanism of sandstone specimens with a hole under compression. Int J Mech Sci 163:105084
35. Johnson KL (1987) Contact mechanics. Cambridge University Press, Cambridge, UK
36. Rao SS (2019) Vibration of continuous systems. John Wiley & Sons, Hoboken, NJ, USA
37. Kazemirad S, Mongeau L (2013) Rayleigh wave propagation method for the characterization of a thin layer of biomaterials. J Acoust Soc Am 133(6):4332–4342
38. Schwarz S, Hartmann B, Sauer J, Burgkart R, Sudhop S, Rixen DJ, Clausen-Schaumann H (2020) Contactless vibrational analysis of transparent hydrogel structures using laser-Doppler vibrometry. Exp Mech 60(8):1067–1078
39. Wang B, Moura AG, Chen J, Erturk A, Hu Y (2020) Characterization of hydrogel structural damping. Extreme Mech Lett 40:100841
40. Parker NG, Povey MJW (2012) Ultrasonic study of the gelation of gelatin: phase diagram, hysteresis, and kinetics. Food Hydrocoll 26(1):99–107
41. Mastrogiannis D, Andreopoulos SI, Potirakis SM (2019) A comparative study by using two different log-periodic power laws on acoustic emission signals from LiF specimens under compression. Eng Fract Mech 210:170–180
42. Tymiak NI, Daugela A, Wyrobek TJ, Warren OL (2003) Highly localized acoustic emission monitoring of nanoscale indentation contacts. J Mater Res 18(4):784–796
43. Minozzi M, Caldarelli G, Pietronero L, Zapperi S (2003) Dynamic fracture model for acoustic emission. Eur Phys J B Condens Matter Complex Syst 36(2):203–207
44. Hagedorn P, DasGupta A (2007) Vibrations and waves in continuous mechanical systems. John Wiley & Sons
45. ElBatanouny MK, Larosche A, Mazzoleni P, Ziehl PH, Matta F, Zappa E (2014) Identification of cracking mechanisms in scaled FRP reinforced concrete beams using acoustic emission. Exp Mech 54(1):69–82
46. Aggelis DG, Mpalaskas AC, Ntalakas D, Matikas TE (2012) Effect of wave distortion on acoustic emission characterization of cementitious materials. Constr Build Mater 35:183–190
47. Pansino S, Taisne B (2020) Shear Wave Measurements of a Gelatin's Young's Modulus. Front Earth Sci 8:171
48. Gokgol C, Basdogan C, Canadinc D (2012) Estimation of fracture toughness of liver tissue: Experiments and validation. Med Eng Phys 34(7):882–891
49. Misra S, Reed KB, Schafer BW, Ramesh KT, Okamura AM (2010) Mechanics of flexible needles robotically steered through soft tissue. Int J Rob Res 29(13):1640–1660
50. Forte AE, D'amico F, Charalambides MN, Dini D, Williams JG (2015) Modelling and experimental characterisation of the rate dependent fracture properties of gelatine gels. Food Hydrocoll 46:180–190
51. Chen C, Fan X, Chen X (2020) Experimental investigation of concrete fracture behavior with different loading rates based on acoustic emission. Constr Build Mater 237:117472
52. Aki K, Richards PG (2009) Quantitative seismology-theory and methods, 2nd edn. University Science books, Sausalito, California (Corr Print)
53. Enoki M, Kishi T (1988) Theory and analysis of deformation moment tensor due to microcracking. Int J Fract 38(4):295–310
54. Yeo A, Kai Y, Che F, Zhou K (2017) Study on damage and fracture of thin-film stacked structures through indentation test with acoustic emission sensing. Int J Mech Sci 128:159–167
55. Jungk JM, Boyce BL, Buchheit TE, Friedmann TA, Yang D, Gerberich WW (2006) Indentation fracture toughness and acoustic energy release in tetrahedral amorphous carbon diamond-like thin films. Acta Mater 54(15):4043–4052
56. Elmquist J (2013) A nonlinear acoustic emission sensor design for monitoring nanoscale material failure. University of Wisconsin-Madison, WI, USA (Master's Thesis)